Journal of Magnetic Resonance 381 (2025) 107990

Contents lists available at ScienceDirect

Journal of Magnetic Resonance

journal homepage: www.elsevier.com/locate/jmr

Magnetic resonance imaging using a straight wire magnetic field for spatial signal encoding: Imaging verification with 2D experiments and 3D modeling

Kaja Tušar [a], Igor Serša [b,c,*]

[a] Jožef Stefan International Postgraduate School, Ljubljana, Slovenia
[b] Jožef Stefan Institute, Ljubljana, Slovenia
[c] Institute of Anatomy, Faculty of Medicine, University of Ljubljana, Ljubljana, Slovenia

ARTICLE INFO

Keywords:
Magnetic resonance imaging
Spatial signal encoding
K-space
Gradient coils
Nonlinear coils
Image reconstruction

ABSTRACT

Spatial encoding in MRI is usually performed using gradient coils that produce a linearly increasing magnetic field B_z in a desired spatial direction such that its gradient is constant. However, it has been shown that spatial encoding in MRI can also be performed with coils that produce nonlinear magnetic fields. In this study, the performance of different types of nonlinear encoding coils, which have a simple design based on the use of a straight wire segment as a building block and a source of a highly nonlinear magnetic field, was experimentally tested in 2D and by simulation in 3D on coils with a nonsymmetric and a symmetric arrangement of these wire segments. All images were reconstructed using our newly presented method, in which the signals are first transformed from the time- to the frequency-domain, yielding a distorted image (spectrum), which is then geometrically and intensity corrected. The quality of the reconstructed images was quantified by comparing them with corresponding reference images obtained with conventional gradient coils. The reconstruction method was accurate for all tested encoding coils and showed that the symmetric coil type produced results that required significantly less corrections compared to the nonsymmetric coil type. Quantitative image quality measurements showed that all encoding coils, despite large differences in the magnetic field of the encoding coils, produce images of similar quality. The results of the study may help advance the design of "gradient" coils towards freer geometries, higher magnetic field gradients or lower inductance and thus faster switching times.

1. Introduction

The first successful MRI experiment was conducted in 1973 by P.C. Lauterbur [1]. This was an image of liquid-filled tubes reconstructed from a set of 1D profiles recorded by increasing the projection angle. In the MRI, this imaging has since been largely replaced by more efficient imaging methods based on multidimensional Fourier transformation reconstruction [2]. Along with these methods, the concept of *k*-space was also introduced, i.e., the spatial-frequency space that is proportional to the temporal integral of the magnetic field gradient. From the analysis presented in [2], it follows that the MR signal as a function of $\vec{k}$ and the MR image as a function of $\vec{r}$ are interconnected by the Fourier transform while forming the $\vec{k}$ and $\vec{r}$ Fourier conjugated pair. This pair in MR imaging replaces an equivalent pair of t and ω in NMR spectroscopy. Parallel imaging accelerates the imaging speed or increases its spatial resolution by combining RF and gradient signal encoding [3–5]. There were also efforts to perform MRI using alternative encoding methods, such as the use of nonlinear magnetic fields generated by special coils, in contrast to the linear magnetic fields produced by conventional gradient coils. Many of such methods, e.g., PatLoc, O-Space, Fronsac and similar [6–9], rely on the use of nonlinear encoding magnetic fields in combination with localized RF receiver sensitivities to deploy additional degrees of freedom from nonlinear magnetic fields for parallel imaging. Important contribution to the understanding of imaging with nonlinear encoding magnetic fields is also provided by the methods for removing image artifacts due to the magnetic field gradient nonuniformity [10–12]. Besides alternative gradient coil designs or no use of gradient coils at all [13], alternative designs of B_0 field magnets are also discussed [14].

* Corresponding author at: Jožef Stefan Institute, Jamova 39, 1000 Ljubljana, Slovenia.
E-mail address: igor.sersa@ijs.si (I. Serša).

https://doi.org/10.1016/j.jmr.2025.107990
Received 22 June 2025; Received in revised form 27 September 2025; Accepted 27 October 2025
Available online 30 October 2025
1090-7807/© 2025 The Authors. Published by Elsevier Inc. This is an open access article under the CC BY license (http://creativecommons.org/licenses/by/4.0/).

Nonlinear magnetic field coils have been employed to enhance 3D imaging in several innovative ways. These coils can be used to enable generating specialized shapes, such as cylindrical regions, which help reduce scan time in 3D imaging [15]. They also facilitate organ-targeted diffusion measurements [16] and enable the excitation of curved slices that conform to specific anatomical structures [17,18]. Additionally, nonlinear coils have been used in MR imaging with unique encoding methods. For instance, fields that are periodic in the *x*-direction and linear in the *y*-direction (PERL) allow for imaging that requires a combination of Bessel function-based and Fourier transform operations [19,20]. Using a Z_2 spherical harmonic magnetic field in conjunction with conventional *x* and *y* gradients permits signal acquisition from O-shaped rings with varying radii and adjustable centers, which can be utilized for parallel imaging without phase encoding (O-space imaging) [8]. A monoplanar gradient system with nonlinear magnetic fields has also been developed as an insert for a 3 T human scanner [21]. Furthermore, nonlinear magnetic field coils play a role in parallel imaging by performing phase scrambling, which speeds up the sensitivity calibration of RF coils [22] and addresses RF coil isosensitivity issues (null-space imaging) [23]. The potential of using nonlinear magnetic field coils alongside conventional gradient coils was also explored to achieve focused imaging in specific regions of the sample (4D-RIO) [24]. In the FRONSAC method, nonlinear coils enhance encoding efficiency by adding a rapidly rotating, moderate-amplitude nonlinear spatial encoding magnetic field to standard linear gradient trajectories [9,25] and can be also used for 3D imaging [26].

Recently we presented a novel method of MR imaging with nonlinear magnetic fields [27]. The general idea of this method stems from the realization that the *k*-space concept has severe limitations if used to reconstruct images from signals encoded with nonlinear coils. These limitations do not exist when the signal is considered as a function of time and the corresponding "image" as the signal's spectrum. However, this "image" is distorted due to nonlinear relationships between the frequency and space of these encoding coils. Therefore, in the second reconstruction step, the "image" needs unwarping using this frequency-to-space relationship to obtain true (undistorted) image. In that study, the proposed reconstruction method was verified with 2D experiments on encoding coils that consisted of a single straight wire segment for each encoding channel.

The present study extends our previous study [27] by investigating the hypothesis that a straight wire segment as a source of a highly nonlinear magnetic field can be used as a building block for simple encoding coils for MR imaging with nonlinear magnetic fields, which have a simple design that allows for analytical mathematical modeling. This hypothesis is demonstrated theoretically and experimentally in 2D by comparing the previously used nonsymmetric arrangement of straight wires [27,28] with a symmetric arrangement of such wires, in which an additional wire is symmetrically placed relative to the existing wire for each encoding channel. This comparison showed that this seemingly very similar coil design results in quite different properties of the encoding coils, with the nonsymmetric arrangement resulting in extreme gradients near the wire and the symmetric arrangement resulting in an almost perfectly uniform gradient in the middle between the wires. In this study, our novel reconstruction method is first briefly introduced, and then this method is applied to reconstruct 2D images of various samples obtained using these two different types of nonlinear encoding coils. The differences between reference images obtained with conventional gradient coils and images obtained with these nonlinear coils are analyzed to evaluate their performance. Finally, this method was also tested for the first time in 3D by computer simulation of imaging with three straight wires arranged in an equilateral triangle, where each of these three wires served as an independent spatial encoding coil.

2. Materials and methods

2.1. MRI using nonlinear pulsed magnetic fields for spatial encoding

Fourier imaging methods, most commonly used in modern MRI, are based on the use of gradient coils for signal spatial encoding and with them closely related concept of *k*-space for image reconstruction. The *k*-space concept evolved from multidimensional spectroscopy by replacing the Fourier transform conjugated pair of frequency ω and time *t* with a pair of space *r* and spatial frequency *k*. In Fourier transform frequency ω and time *t* are two independent variables and in order to preserve the structure of the Fourier transform, these two variables must be replaced with another pair of independent variables. In the case of gradient coils, they are conveniently substituted by a pair of *r* and *k*, where these two are derived from ω and *t* using the relation

$$\omega t = \left(\gamma\vec{G}\cdot\vec{r}\right)t = \vec{r}\cdot\left(\gamma\vec{G}t\right) = \vec{r}\cdot\vec{k} \tag{1}$$

in which ω corresponds to *r* and *t* corresponds to *k*

$$\omega\rightarrow\vec{r} \quad , \quad t\rightarrow\vec{k} = \gamma\vec{G}t \tag{2}$$

This substitution is possible because gradient coils produce a linearly increasing magnetic field $B_z = B_0 + \gamma\vec{G}\cdot\vec{r}$, which has a constant gradient $\vec{G} = \nabla B_z$. If gradient coils are replaced by nonlinear magnetic field coils for spatial encoding in MRI, then such a substitution is not possible because *k* and *r* are, in the case of these coils, not independent, i.e., the magnetic field gradient is not constant

$$\vec{G}(\vec{r}) = \nabla B_z(\vec{r}) \tag{3}$$

A consequence of Eq. (3) is that *k*, as defined previously in Eq. (2), is also a function of *r* [6; 7]

$$\vec{k}(\vec{r}) = \gamma\vec{G}(\vec{r})t \tag{4}$$

which precludes the use of *k*-space concept for image reconstruction when the signal is spatially encoded with nonlinear magnetic field coils. However, ω and *t* are still independent variables even when using the nonlinear coils for signal encoding. This reasoning leads us to consider the encoded signal as a function of multidimensional time, and the reconstructed image as a derivative of the corresponding multidimensional spectrum. Specifically, the signal of a sample with a proton density $\rho(\vec{r})$ can be written as

$$S(\vec{t}) = \int \rho(\vec{r})\exp\left(i\vec{\omega}(\vec{r})\cdot\vec{t}\right)d\vec{r} \tag{5}$$

relaxation and off-resonance effects are here neglected. Eq. (5) reminds of a Fourier transform, but it is not, because of the integration over $\vec{r}$ instead of over $\vec{\omega}$. However, such integration can be performed if a substitution of variables is applied to Eq. (5)

$$S(\vec{t}) = \int \rho(\vec{r}(\vec{\omega}))\exp\left(i\vec{\omega}\cdot\vec{t}\right)\left|\frac{\partial\vec{r}}{\partial\vec{\omega}}\right|d\vec{\omega} \tag{6}$$

Factor $|\partial\vec{r}/\partial\vec{\omega}|$ in Eq. (6) is known as the Jacobian determinant. Eq. (6) can now be inverted using the inverse Fourier transform

$$\rho(\vec{r}(\vec{\omega}))\left|\frac{\partial\vec{r}}{\partial\vec{\omega}}\right| = \widehat{S}(\vec{\omega}) = \frac{1}{(2\pi)^D}\int S(\vec{t})\exp\left(-i\vec{\omega}\cdot\vec{t}\right)d\vec{t} \tag{7}$$

here $\widehat{S}(\vec{\omega})$ is the multidimensional spectrum and *D* is the dimensionality of the transform. The result of Eq. (7) enables the calculation of the MR image using the relation

$$\rho(\vec{r}) = \widehat{S}(\vec{\omega}(\vec{r}))\left|\frac{\partial\vec{\omega}}{\partial\vec{r}}\right| \tag{8}$$

In Eq. (8) the relation between Jacobian determinant and its inverse was used $|\partial\vec{r}/\partial\vec{\omega}| = 1/|\partial\vec{\omega}/\partial\vec{r}|$. The calculation of the image from the spectrum in Eq. (8) is possible when the transformation between $\vec{r}$ and $\vec{\omega}$ is bijective, so that each $\vec{r}$ in the sample region transforms to one $\vec{\omega}$ of the spectrum and vice versa. This is possible when for these values of $\vec{r}$ the Jacobian determinant (or of $\vec{\omega}$ for the inverse Jacobian determinant) is continuously differentiable and always nonzero. Eq. (8) can also be interpreted as an equation that defines corrections of the distorted "image" $\widehat{S}(\vec{\omega})$ to the undistorted image $\rho(\vec{r})$. These corrections are the unwarping by converting the frequency coordinates to the corresponding spatial coordinates by the transformation $\vec{\omega}(\vec{r})$ in the first factor of Eq. (8), and the intensity corrections by the Jacobian determinant in the second factor of Eq. (8).

The frequency vector $\vec{\omega}(\vec{r}) = (\omega_1(\vec{r}), \cdots, \omega_D(\vec{r}))$ in Eqs. (5)–(8) has components that correspond to nuclear precession frequency shifts generated by magnetic fields of each of $i = 1 \ldots D$ nonlinear coils

$$\omega_i(\vec{r}) = \gamma I_{ref,i}(B/I)_i(\vec{r}) \tag{9}$$

Here B/I denotes magnetic field of the coil that it generates per unit of current and I_{ref} is the reference current through this coil. In case of the time vector $\vec{t} = (t_1, \cdots, t_D)$ its components are defined as the time integral of the actual current through the encoding coil divided by the corresponding reference current

$$t_i = \frac{1}{I_{ref,i}}\int I_i(t)\,dt \tag{10}$$

In Eq. (10), the integration interval corresponds to the time interval between the excitation of the signal and the recording of the signal. If the imaging sequence includes refocusing RF pulses, then the integral in Eq. (10) must be split in more integrals in intervals that end before and start after each of the refocusing pulses. These integrals are then summed with signs of -1 to the power equal to the number of refocusing pulses to the signal recording.

2.2. Construction of nonlinear spatial encoding coils for 2D MRI

Nonsymmetric and symmetric nonlinear coil designs are based on a coil in the form of a square loop, of which two longer segments of length $l = 117$ mm are parallel to the static magnetic field, and two shorter segments of length $2a = 43.2$ mm are perpendicular to it and have a direction along the x or y axis (Fig. 1). One of these segments, i.e., the active segment, lies in the imaging plane, and the other is well out of it, so that its magnetic field in the imaging plane can be neglected. In the case of the nonsymmetric coil design, the coil has only one such square loop for each channel, while in case of the symmetric coil design it has two such loops located symmetrical with respect to z-axis; the loops are off-center by a distance $r = 25.2$ mm. The frame for these coils was printed from ABS plastic using a 3D printer (Prusa, Prague, Czech Republic). The frame contained 2.8×2.8 mm^2 channels for square coils, in which 50 turns of enameled copper wire with a diameter of 0.15 mm and a total resistance of 15 Ω were wound in the case of nonsymmetric coils and 30 turns of enameled copper wire with a diameter of 0.4 mm and a total resistance of 2.6 Ω were wound in the case of symmetric coils. The windings were fixed in the channel with a two-component epoxy adhesive (UHU Plus 90 min, UHU GmbH, Bühl/Baden, Germany). These encoding coils were designed to be compatible with existing Bruker microimaging accessories (Bruker, Ettlingen, Germany) as seen in Fig. 2; they could be connected directly to existing Bruker gradient microimaging amplifiers, while a copper RF shield had to be installed in the internal bore of the frame to allow the use of existing Bruker RF microimaging coils.

2.3. Test samples

Validity of the presented theory for image reconstruction from signals spatially encoded with nonlinear magnetic field coils and the performance of the encoding coils were evaluated using two artificial test samples and one biological sample. The artificial test samples were disc-shaped with a checkerboard 2 mm by 2 mm pattern or with letters "a"

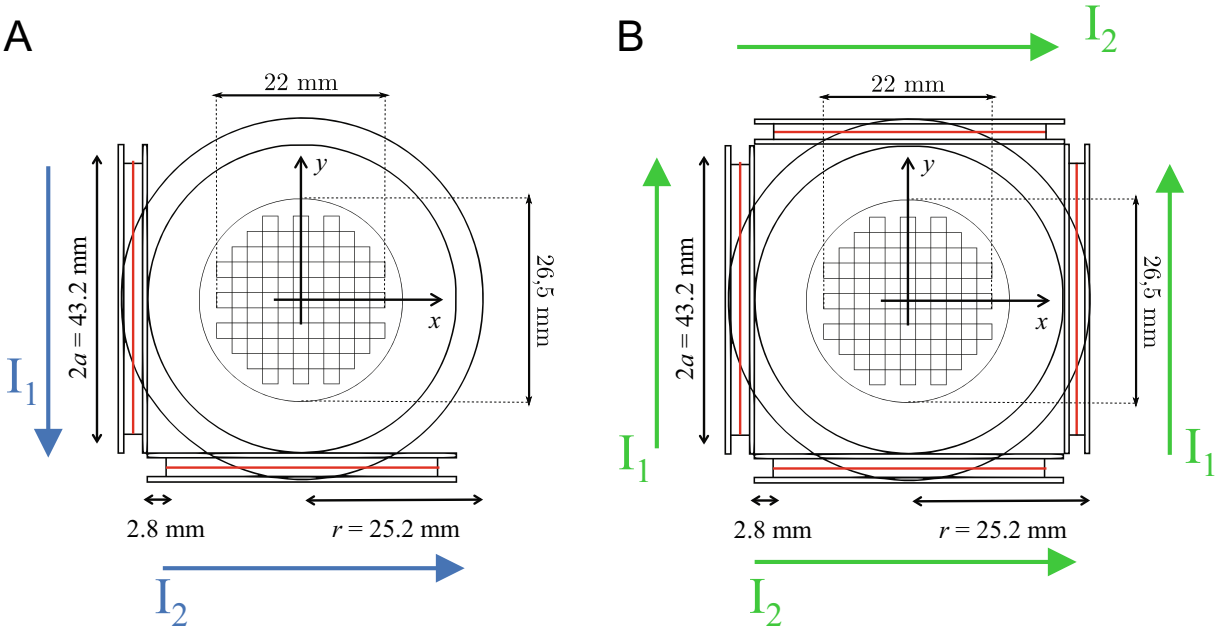

Fig. 1. A schematic drawing of the encoding coils with the inserted test sample. The nonsymmetric encoding coil array (A) features two separate coils, each with just one straight wire segment with current. The segments of the coils are oriented perpendicular to each other. The symmetric encoding coil array (B) also includes two separate coils, perpendicular to each other, but each segment of the nonsymmetric coils now has its symmetrically placed opposite segment with current in the same direction.

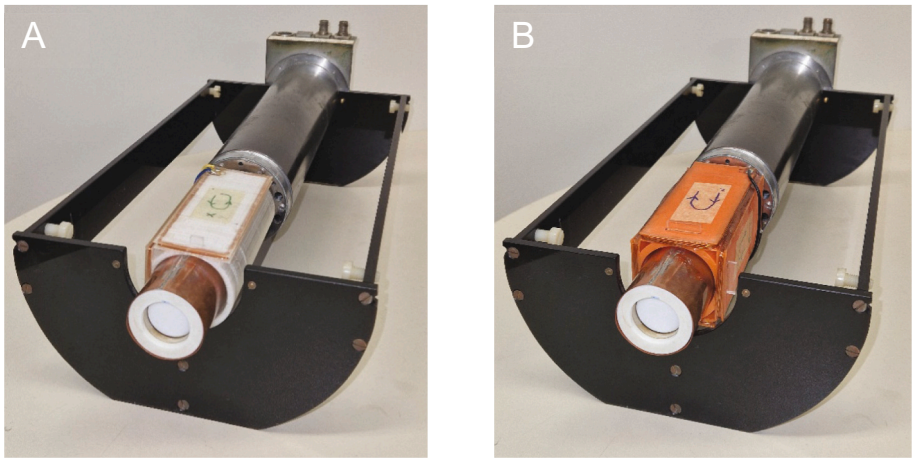

Fig. 2. Nonsymmetric (A) and symmetric (B) nonlinear magnetic field coils are constructed from one off-center (nonsymmetric) or two symmetrically placed square loops for each of the two channels. The coils are made of enameled copper wire wound into the corresponding channels on a 3D printed plastic frame. The photos show the magnetic field encoding coils with the RF coil, both mounted in a microimaging probe holder.

and "b" recessed 2 mm in the 3 mm thick disk with 26.6 mm diameter (Fig. 3A). The artificial test samples were 3D-printed using a UV-curable resin printer (Prusa, Prague, Czech Republic) and the cavities of the printed discs were then filled with a moisturizing cream (Nivea, Hamburg, Germany), which produced an optimal NMR signal for imaging (Fig. 3B). The biological sample was a 4 mm thick slice of strawberry with an approximate diameter of 25 mm. The strawberry sample was wrapped in cellophane foil before imaging to prevent it from drying out during imaging.

2.4. 2D MRI using nonlinear magnetic field coils for spatial signal encoding

MR imaging was conducted using both linear (gradient) and nonlinear magnetic field spatial encoding coils with standard MRI equipment, which included a superconducting 2.35 T (100 MHz proton frequency) horizontal-bore high-resolution NMR magnet (Oxford Instruments, Abingdon, UK), a digital NMR/MRI spectrometer (Tecmag, Houston, TX, USA), and RF and gradient accessories for MR microscopy (Bruker, Ettlingen, Germany). The samples were scanned in a 27 mm transmit/receive RF coil and with original 250 mT/m gradient coils or with previously described nonsymmetric or symmetric nonlinear encoding coils that were all connected directly to 10 A gradient amplifiers.

Each sample was first scanned by a spin-echo imaging sequence using conventional gradient coils and imaging parameters: field of view (FOV) 50 mm, readout gradient (G_r) 23.5 mT/m, phase gradient amplitude (G_{p_max}) 20 mT/m, phase gradient pulse duration (t_p) 3 ms, imaging matrix ($N \times N$) 256 × 256, dwell time (Δt) 20 μs, acquisition frequency bandwidth (BW_1) 50 kHz, repetition time (TR) 530 ms, echo time (TE) 26 ms. Then, the gradient coils were replaced with nonsymmetric and finally with symmetric nonlinear magnetic field coils, while the sample in the RF probe remained intact both times. For imaging with these two coil types, all the time parameters of the spin-echo sequence remained unchanged, while gradient amplitudes were replaced by the corresponding current amplitudes for each of the two channels.

For each channel i must be met a condition that the acquisition frequency bandwidth BW_i is higher or equal to the nuclear precession frequency range $\Delta\omega_i$ of the object when the reference current $I_{ref,i}$ is flowing through the encoding coil i

$$BW_i = \frac{1}{\Delta t_i} \geq \Delta\omega_i \tag{11}$$

Note that the acquisition frequency bandwidth BW_i is also equal to reciprocal acquisition dwell time Δt_i. For the frequency-encode channel (channel 1), the reference current is already the actual through the corresponding coil

$$I_1 = I_{ref,1} \tag{12}$$

While for the phase-encode channel (channel 2), the dwell time parameter $\Delta t_2 = 1/BW_2$ and the reference current $I_{ref,2}$ can be used to calculate the phase-encode current increase step and the phase current amplitude. These are equal to

$$\Delta I_2 = I_{ref,2}\Delta t_2/t_p \quad , \quad I_{2\_max} = \Delta I_2 N/2 \tag{13}$$

according to Eq. (A.2).

All experiments were performed with $BW_1 = BW_2 = 50$ kHz and

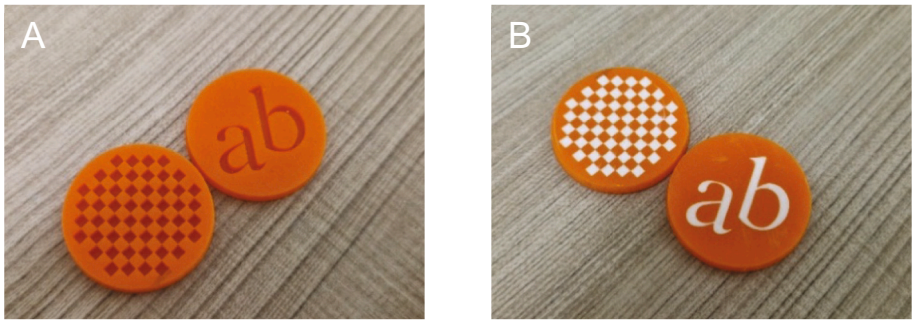

Fig. 3. Test samples were prepared from 3D-printed plastic discs that had a checkered pattern or a pattern of the letters "a" and "b" recessed 2 mm into the disc (A). The sample was later filled with a moisturizing cream (B), which provided the NMR signal for imaging.

$\Delta t_1 = \Delta t_2 = 20\ \mu$s. Due to the identical construction of coil 1 and coil 2, which applies to both types of encoding coils, and the round shape of the samples, Eq. (11) yielded identical reference currents for both channels. These were equal to $I_{ref,1} = I_{ref,2} = 70.8$ A for nonsymmetric encoding coils and were equal to $I_{ref,1} = I_{ref,2} = 35.0$ A for symmetric encoding coils. The actual currents through the coils were then determined using Eqs. (12), (13) which yielded $I_1 = 70.8$ A, $\Delta I_2 = 0.472$ A and $I_{2\_max} = 60.4$ A for nonsymmetric encoding coils and $I_1 = 35.0$ A, $\Delta I_2 = 0.233$ A and $I_{2\_max} = 29.9$ A for symmetric encoding coils. Note that these currents correspond to the total current of the wires of all coil turns, while the actual current through an individual coil wire was 50 times and 30 times smaller for the nonsymmetric and symmetric coil, respectively.

2.5. Simulation of 3D MRI using nonlinear magnetic field coils for spatial signal encoding

In this imaging simulation, three independent infinitely long straight wires were used, each serving as an independent spatial encoding coil for MRI. The wires were arranged in an equilateral triangle in the *xy* plane at $z = 0$, as shown in Fig. 4A. In this simulation, the side *s* of the triangle was 15 cm, and the reference current through each wire was $I_{ref,1} = I_{ref,2} = I_{ref,3} = 100$ A. The center of this triangle was centered at the origin of the coordinate system. The channel 1 wire was aligned with the *x* axis, and the channel 2 and 3 wires were at an angle of $-60°$ and $60°$ to this axis. The imaging field of view (FOV) was set to the ranges [−FOV/2, FOV/2], [−FOV/2, FOV/2], and [0, FOV] for the *x*, *y*, and *z* axes, respectively. In the simulation, the FOV was set to 3 cm. Imaging matrix was equal to $(N \times N \times N)$ $64 \times 64 \times 64$ and signal acquisition was performed with a bandwidth $BW_1 = BW_2 = BW_3 = 12.5$ kHz. Signals of frequencies in the range from 12.5 kHz to 25 kHz were acquired for all three frequency components.

In the first step of the simulation, a reference (test) image was used to calculate the spectrum using the inverse equation to Eq. (8), i.e., $\hat{S}(\vec{\omega}(\vec{r})) = \rho(\vec{r})/|\partial\vec{\omega}/\partial\vec{r}|$ and in the second step Eq. (8) $(\rho(\vec{r}) = \hat{S}(\vec{\omega}(\vec{r}))|\partial\vec{\omega}/\partial\vec{r}|)$ was used to calculate a reconstructed image from the spectrum. Magnetic fields of the coils and thus their transformation of spatial to frequency coordinates was calculated using Eq. (C.2) and the corresponding Jacobian determinant using Eq. (C.4). For the reference image was used a micro MR image of a small walnut that was acquired on the MR system described in 2.6 using the 3D spin-echo method at the FOV 3 cm and matrix $64 \times 64 \times 64$.

2.6. Image reconstruction and processing

The acquired MR image signal in the time domain was first Fourier transformed into the multidimensional spectrum using TNMR signal acquisition and processing software (Tecmag, Houston, TX, USA). The spectrum, that represented distorted "image", was then reconstructed in the undistorted image using geometrical and intensity corrections given in Eq. (8). The most challenging part of this calculation was the unwarping procedure, which in this study was performed by assigning each spatial discrete coordinate the value of the closest transformed frequency coordinate. The spatial coordinates lay on a rectangular grid, and the frequency coordinates, transformed into the corresponding spatial coordinates, lay on a warped grid. Image reconstruction programs were implemented as macro programs in ImageJ image processing software (NIH, Bethesda, MD, USA). These macro programs were developed by the authors of this study.

The alignment between the reconstructed and reference images was quantified using the Cross-Correlation (CC) metric, defined as

$$CC = \frac{\sum_{ij} A_{ij} \cdot B_{ij}}{\sqrt{\sum_{ij} A_{ij}{}^2 \cdot \sum_{ij} B_{ij}{}^2}} \tag{14}$$

here, *A* and *B* represent the image matrices, while *i* and *j* denote the pixel indices within the images. In addition to the Cross-Correlation metric, the Structural Similarity Index Metric (SSIM) [29] and the Peak Signal-to-Noise Ratio (PSNR) metric [30] were also used to evaluate the fidelity of reconstructed images. The latter two metrics were found among the ImageJ plugins and were used with their default parameters.

3. Results

3.1. 2D MRI using nonsymmetric and symmetric nonlinear spatial encoding coils

The Jacobian determinant $|\partial\vec{\omega}/\partial\vec{r}|$ (the second factor in Eq. (8)) plays a very important role in image reconstruction from signals encoded by nonlinear coils. It is responsible for correcting the signal intensity, which varies due to the spatially varying space-to-frequency transformation.

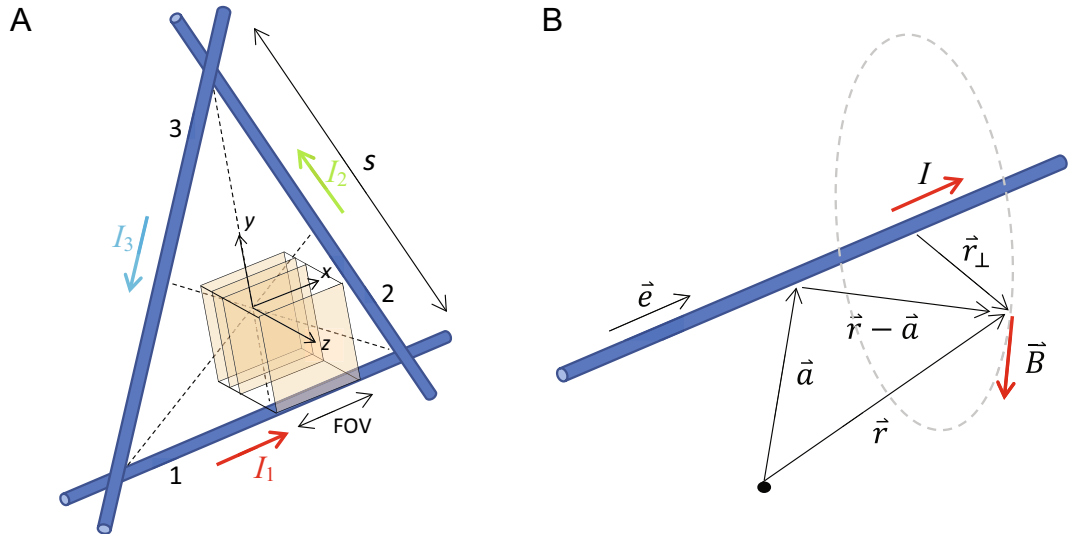

Fig. 4. The arrangement of three straight wires in an equilateral triangle that can serve as a system for spatial signal encoding in 3D imaging (A) and schematic of the vectors in Eq. (C.1) for calculating the magnetic field around an infinitely long straight wire (B). The wires lie in the *xy* plane at $z = 0$. The imaging field of view (FOV) is a cube with the bottom side in this plane and centered at FOV/2 above the center of the triangle.

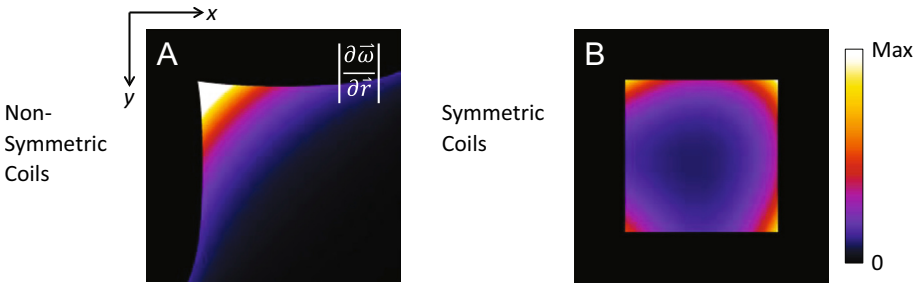

Fig. 5. Plots of the Jacobian determinant as a function of space for nonsymmetric encoding coils (A) and symmetric encoding coils (B). These two types of coils have a distinctly different spatial dependence of the Jacobian determinant, from which the differences in symmetry between these two coil types are also clearly evident.

Since this transformation is an inherent property of the encoding coil, so is the corresponding Jacobian determinant. Fig. 5 depicts plots of the Jacobian determinant as a function of space for both types of encoding coils (nonsymmetric and symmetric). The properties of symmetric encoding coils, such as the presence of an isocenter and a relatively uniform magnetic field gradient in the region between wire segments are also reflected in the corresponding Jacobian determinant (Fig. 5B), which is also relatively uniform between the wires and begins to deviate from this in the vicinity of the wires. In the case of nonsymmetric encoding coils, the Jacobina determinant (Fig. 5A) is significantly different. It is very uniform due to the fact that the magnetic field gradient of this type of coil is nonconstant and increases sharply in the vicinity of the wires. In this region, the Jacobian determinant is the highest. The absence of an isocenter in these coils is reflected in the absence of the local minimum of the Jacobian determinant. The Jacobian determinants in Fig. 5 were used in the reconstructions of all the images presented below.

The performance of three different spatial encoding coils, conventional gradient coils, nonsymmetric coils, and symmetric coils, was tested first on the checkerboard test sample. Results of imaging with these coils are shown in Fig. 6. The reference image in Fig. 6A was obtained by using conventional gradient coils. With these coils, the spectrum represents already an undistorted image of the sample. When using nonlinear coils for spatial signal encoding, the spectrum represents a distorted image of the object, which must be further processed by unwarping and intensity corrections given in Eq. (8) to obtain an undistorted image of the object. It can be clearly seen that the needed corrections are considerable for nonsymmetric coils (Fig. 6B, C) and only moderate for symmetric coils (Fig. 6D, E). It can be also seen that the reconstructed images with both nonlinear encoding coils (Fig. 6C, E) match well with the reference image (Fig. 6A). The spectrum obtained using nonsymmetric encoding coils (Fig. 6B) also shows extreme differences in the magnifications of different squares of the checkerboard pattern. This is due to the very different magnetic field gradients at the locations of these squares. Those in a higher magnetic field gradient appear larger and less intense in the spectrum than those in a lower magnetic field gradient. The spectrum obtained using symmetric encoding coils (Fig. 6B) does not show such differences in square magnifications, indicating that these coils produce a more uniform magnetic field gradient.

In the next experiment, the test sample with pattern of letters “ab” was imaged and its results are shown in Fig. 7 with the same five types of images as in the previous experiment. The spectrum of signals encoded with the nonsymmetric coils in Fig. 7B reveals that the regions of the object “ab” that are closer to the coil are mapped to the higher-frequency parts of the spectrum at higher magnification, while the regions farther from the coil are mapped to the lower-frequency parts of it at lower magnification. Similar behavior, but to a lesser extent, can also be seen in the spectrum of signals encoded with the symmetric coils in Fig. 7D. This spectrum has both positive and negative frequencies, where the higher frequencies correspond to the regions closer to the right and lower segments of the coil, and the lower frequencies correspond to its

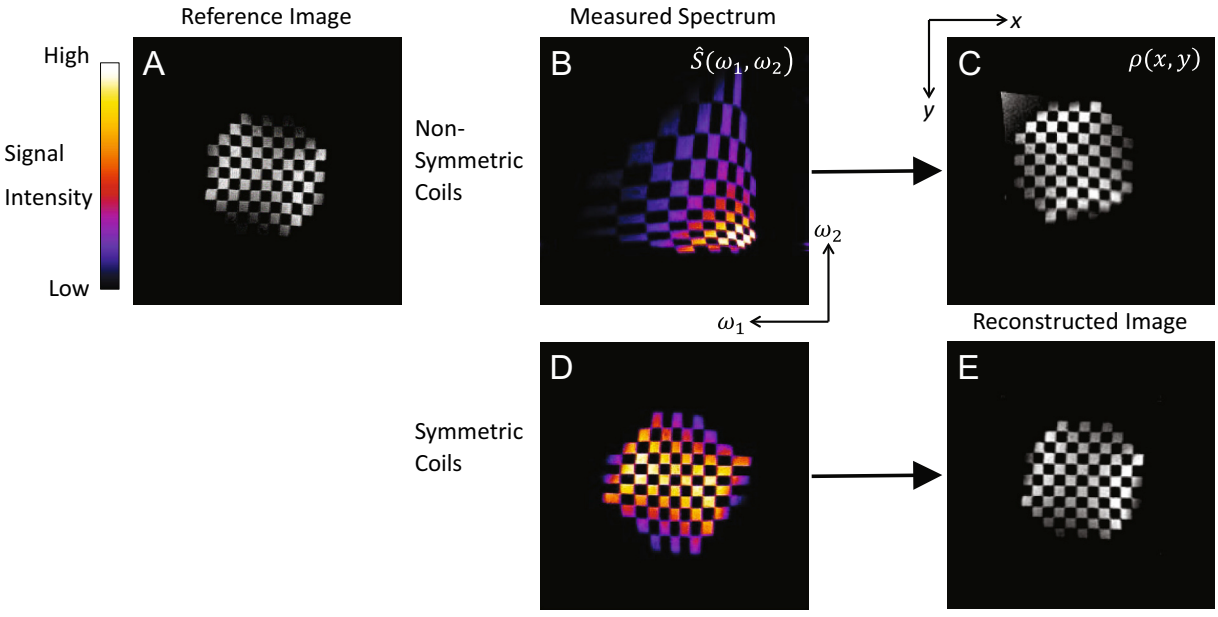

Fig. 6. MR images of the checkerboard test sample: reference image (A) obtained using conventional gradient coils, spectra obtained using nonsymmetric (B) and symmetric (D) encoding coils, and the corresponding reconstructed images for nonsymmetric (C) and symmetric (E) coils.

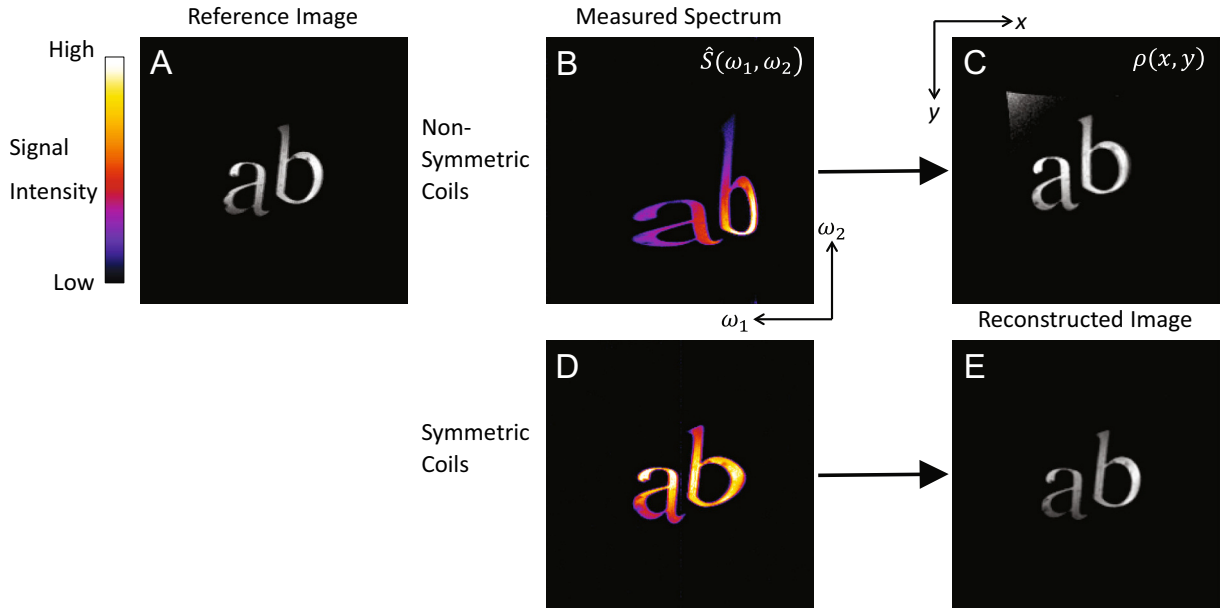

Fig. 7. MR images of the letter "ab" test sample: reference image (A) obtained using conventional gradient coils, spectra obtained using nonsymmetric (B) and symmetric (D) encoding coils, and the corresponding reconstructed images for nonsymmetric (C) and symmetric (E) coils. The reconstructed images have uneven resolution and noise; regions with higher resolution have more noise, while regions with lower resolution have less noise.

left and upper segments. Again, regions of the object that are closer to the coil are magnified more. This variation in magnification affects the reconstructed image, leading to lower resolution in parts of the object that are further from the coil. This effect is noticeable in Fig. 7C, where the lower part of the letter "b" has a jagged outline, and to a lesser extent in Fig. 7E, where the distortion is reduced due to the use of a symmetrical coil with a more uniform magnetic field gradient. Fig. 7C, E show that the noise in the reconstructed images is nonuniform; it is higher in regions with higher resolution and lower in regions with lower resolution.

As a final test, the feasibility of imaging with nonlinear magnetic field coils was evaluated using a slice of a strawberry as a biological sample, with the results presented in Fig. 8. The image obtained using conventional gradient coils in Fig. 8A serves as a baseline for comparison with images obtained using nonlinear coils (Figs. 8B-8E). The spectra in Fig. 8B, D, which were obtained using nonsymmetric and symmetric encoding coils, respectively, were used to reconstruct the corresponding images in Fig. 8C, E. The reconstructed image in Fig. 8C has better resolution in the upper left part, which is closer to the wires and thus in the region of higher magnetic field gradient, than in the lower right part, which is further from the wires, where the magnetic field gradient is lower. The reconstructed image in Fig. 8E has slightly better resolution in the outer regions than in the central ones due to the slightly larger magnetic field gradient there, but the different is not as large as in the case of nonsymmetric encoding coils (Fig. 8C).

It is evident that there is a strong resemblance between the reference

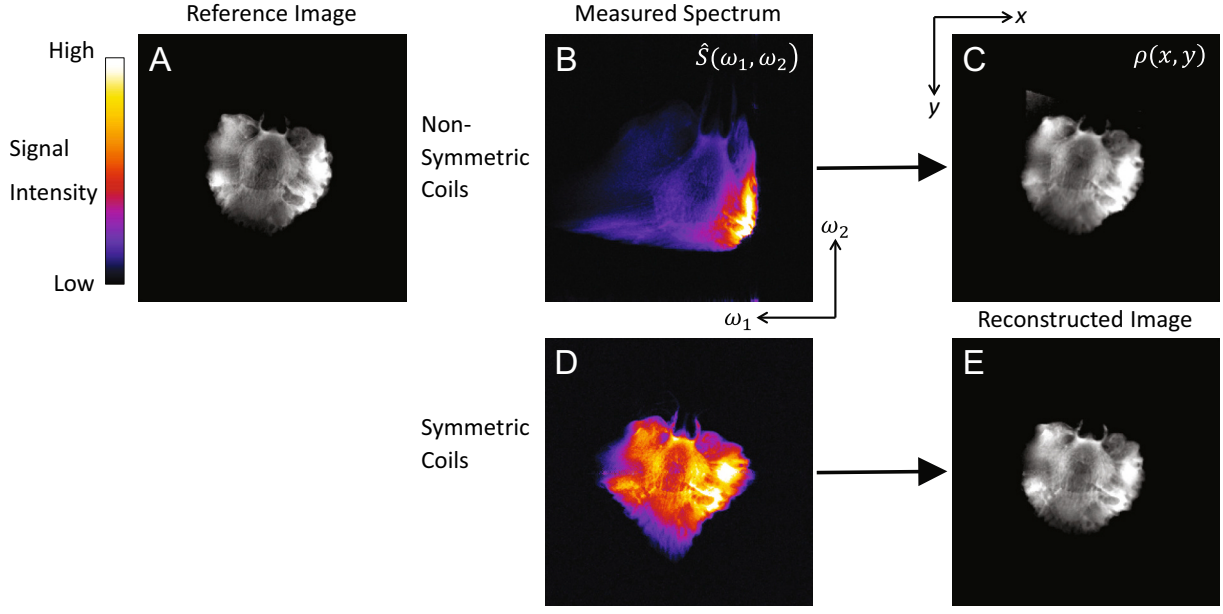

Fig. 8. MR images of a strawberry slice as a biological test sample, represented by: reference image (A) obtained using conventional gradient coils, and spectra (B), (D) and reconstructed images (C), (E) obtained using nonsymmetric (B), (C) and symmetric (D), (E) nonlinear encoding coils. The reconstructed images have uneven resolution due to the use of nonlinear encoding coils. The differences in resolution are more obvious with nonsymmetric coils than with symmetric coils.

images in Figs. 6A, 7A, 8A and the corresponding reconstructed images obtained using nonsymmetric coils in Figs. 6C, 7C, 8C, and symmetric coils in Figs. 6E, 7E, 8E. The reconstructed images closely match the reference images in terms of size, geometry, and intensity, indicating that the imaging process accurately preserves key features of the sample across different experimental setups. This consistency across multiple tests suggests that nonlinear magnetic field coils effectively complement the conventional gradient coils, maintaining the integrity of the reconstructed images, while allowing for the exploration of alternative coil geometries.

Table 1 presents the results of the quantitative analysis of image alignment between the reconstructed and corresponding reference images, as measured by the Cross-Correlation (CC) defined in Eq. (14) as well as by the Structural Similarity Index Metric (SSIM) [29] and the Peak Signal-to-Noise Ratio (PSNR) metric [30]. Before testing, the colocalization (translational and rotational) between the reference and reconstructed images was performed using ImageJ program. As can be seen from the table, image alignment measured by CC is the best (more than 0.95) for the letter "ab" and the strawberry test samples. No significant difference in image alignment was found between the images obtained using nonsymmetric and symmetric encoding coils. For the SSIM metric, the accuracy of the reconstructed image is best for the strawberry test sample and the lowest for the letter "ab" test sample and symmetric coil. The latter can be explained by the sensitivity of SSIM to localized structural differences due to slight residual geometric distortions and local intensity variations, which have only a minor effect on global measures such as CC and PSNR. The PSNR metric, it is best for the same test sample and the symmetric coil type.

3.2. Simulation of 3D MRI using three infinite straight wires arranged in an equilateral triangle

For the experimental setup shown in Fig. 4A, simulations of the precession frequency shift as a function of spatial coordinate were first performed. These are shown in Fig. 9 for all three infinitely long straight wires used as encoding coils: in panel A for coil 1, in panel B for coil 2, and in panel C for coil 3. The frequencies correspond to reference currents of 100 A through each of the coils and are shown in the range from 0 to 37 kHz using color-coding. Fig. 9D shows the corresponding negative of the Jacobian determinant using color-coding. The values shown range from 0 to $2.67{\cdot}10^{19}$ m^{-3} s^{-3}. The spatial coordinates of the displayed maps range from −15 to 15 mm for the x and y axes and from 0 to 30 mm for the z axis. Every other slice (32 out of a 64 total) is shown.

Fig. 10 shows the results of the simulated 3D spectrum and the 3D image of the digital test sample (reference image). The latter is shown in Fig. 10A and represents an image of a small walnut, scanned at a 30 mm FOV with an isotropic spatial resolution of 470 μm. Fig. 10B shows the corresponding calculated spectrum of the test sample, shown with color coding. As could be expected from the frequency maps of the encoding coils in Fig. 9A–C, the frequencies of the test sample are in the range between 12.5 and 25 kHz for all three encoding directions. A similar effect as in 2D can be observed here, namely, the areas of the sample that are closer to the wire are transformed to higher frequency coordinates and are visible in the spectrum as magnified and less intense than the areas of the sample that are further away from the wire, which are transformed to lower frequency coordinates and are visible in the spectrum as less magnified and brighter areas. Fig. 10C shows the reconstructed image from the spectrum. This image no longer has the geometric and intensity distortions that were visible in the spectrum and is very similar to the reference image. A closer inspection would reveal small deviations from the reference image, especially in the regions reconstructed from the lower frequency parts of the spectrum, where the sample depicted in the spectrum does not have sufficient resolution.

Table 1
Results of the cross-correlation (CC), structural similarity index metric (SSIM) and peak signal-to-noise ratio (PSNR) measures to test the similarity between reconstructed images and the corresponding reference images.

Test sample	Coil type	Compared image pair	CC	SSIM	PSNR
Checkerboard	Nonsymmetric	6A vs. 6C	0.842	0.712	18.8
	Symmetric	6A vs. 6E	0.934	0.737	22.9
Letters "ab"	Nonsymmetric	7A vs. 7C	0.957	0.806	23.9
	Symmetric	7A vs. 7E	0.955	0.688	26.8
Strawberry	Nonsymmetric	8A vs. 8C	0.953	0.853	17.7
	Symmetric	8A vs. 8E	0.954	0.868	17.5

4. Discussion

A current flowing through an infinitely long straight wire creates a magnetic field and its gradient of $1/\rho$ and of $-1/\rho^2$ spatial dependencies, where ρ is the radial distance from the wire. In this study, this type of magnetic field was used as a building block in the construction of spatial encoding coils, with the nonsymmetric coil having one such segment and the symmetric coil having two. This type of magnetic field has singularity at the point of the wire $\rho \to 0$ where the magnetic field and its gradient go to infinity. This effect is common to both types of coils and is visible in the spectra as regions of high magnification and lower intensity of the sample image, while these regions have transformed into regions of higher resolution and lower SNR in the corresponding reconstructed images. Sample regions further from the coil have the opposite effect, i.e., lower magnifications and higher signal in the spectra and lower resolution and higher SNR in the reconstructed images. This effect is particularly evident in spectra and reconstructed images obtained using nonsymmetric coils, while it is largely reduced in images obtained with symmetric coils. This is because in symmetric coils, a decrease in the magnetic field of one segment of wire is compensated by an increase in the magnetic field of the opposite segment of wire. Symmetric coils have a magnetic field of zero at the center, so these coils have an isocenter just like conventional gradient coils. Furthermore, their magnetic field in the central region is quite well linear; it is proportional to $1/(\rho + r) + 1/(\rho - r) \approx -2\rho/r^2$ so that its gradient is there constant (proportional to $-2/r^2$), where 2r is the distance between the wire segments.

Experiments with all three different test samples showed that both tested nonlinear magnetic field coils, which were used for spatial encoding of image signals, yielded reconstructed images of similar quality. This can be determined by visually inspection of the images in Figs. 6, 7, 8 and is also indicated by the results of the quantitative cross-correlation test in Table 1. These results prove that the presented theory for image reconstruction of signals encoded with nonlinear coils is correct and also that such imaging can be performed with a wide range of different nonlinear encoding coils. The latter is especially important, as it enables MRI with nonlinear encoding coils optimized for specific needs, e.g., coils of special geometry in cases of limited space, which can also allow for a different design of MRI magnets with more patient-friendly access or optimization of these coils for lower inductance and thus faster switching times and consequently faster imaging.

In the case of nonlinear encoding coils, in the generally accepted k-space formalism, k would become a function of space. This is because nonlinear encoding coils general have a nonconstant gradient of their magnetic field. This precludes the use of the standard Fourier transform for image reconstruction. In the proposed method, however, a substitution is used in the general equation for the signal Eq. (5), namely, the spatial coordinate is replaced by frequency and the k-coordinate by generalized time [27]. This substitution simplifies the phase factor to $\exp(i\vec{\omega}\cdot\vec{t})$ and thus enables the use of standard Fourier transformation to reconstruct the spectrum from time-domain data, which is the first step of reconstruction. This spectrum can be considered a distorted image and is transformed to reconstructed (undistorted) image in the second

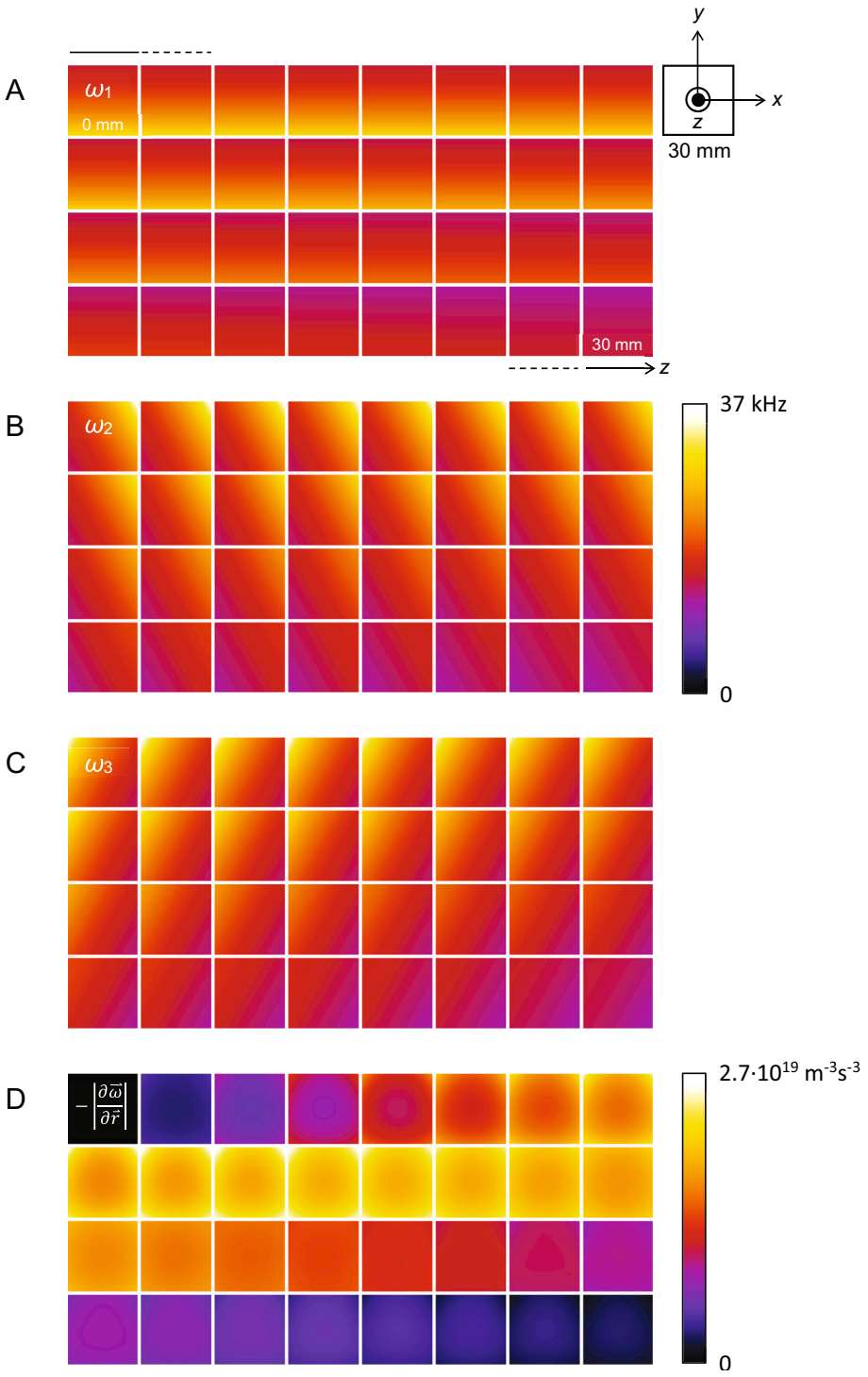

Fig. 9. Precession frequency shift due to 100 A current through encoding coil 1 (A), coil 2 (B), and coil 3 (C) for 3D imaging (Fig. 2B) as a function of position within a 30 mm field of view (FOV) and the corresponding negative of the Jacobian determinant for these frequency shift maps (D).

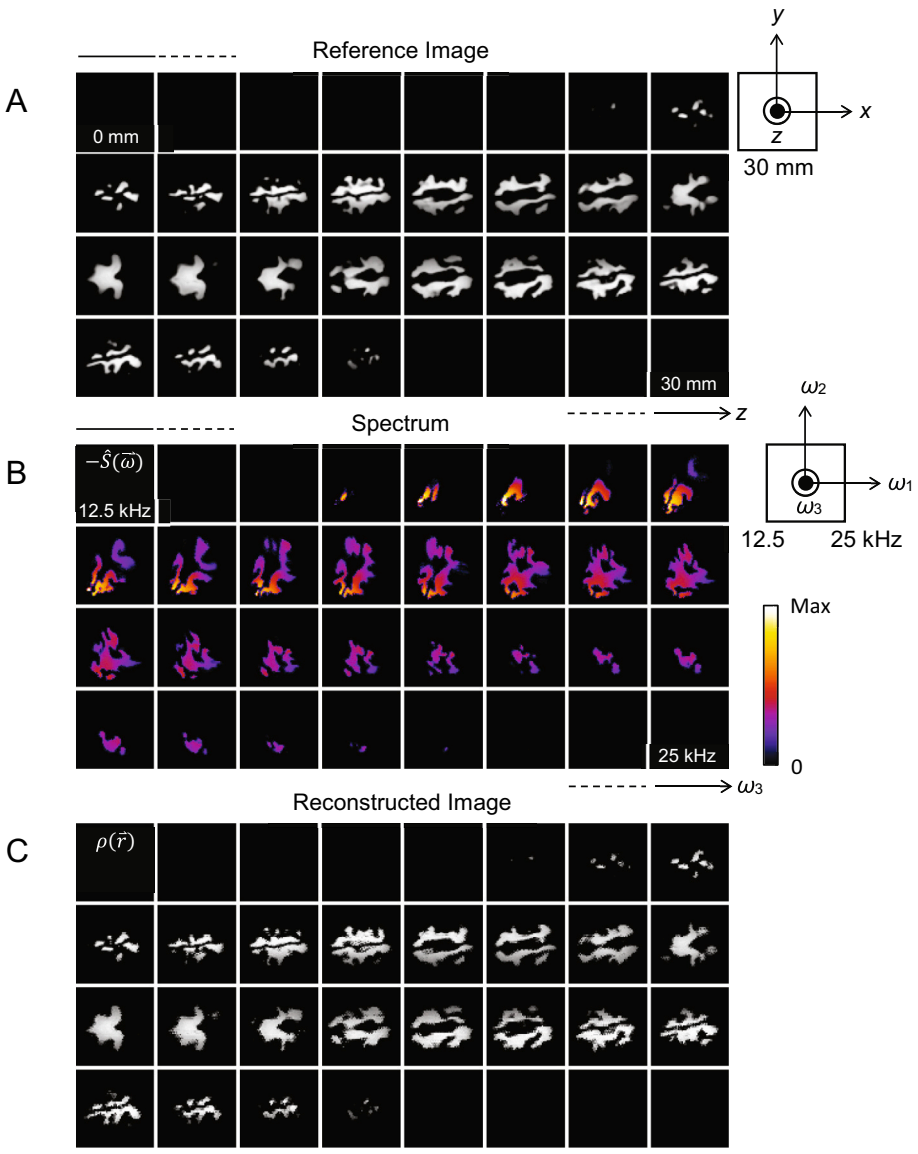

Fig. 10. Computer simulation of 3D imaging with spatial encoding coils in Fig. 2B, shown with the reference image (A), its spectrum (B), and the corresponding reconstructed image (C). The refence image is a 3D image of a walnut that was acquired prior to this study using conventional gradient coils. The spectrum represents the simulated Fourier transformed time-domain signals of the reference sample. It was calculated from the reference image using the inverse of Eq. (8). The final image is reconstructed from the spectrum using Eq. (8).

reconstruction step, which includes geometric and intensity corrections of the spectrum in Eq. (8). Geometric corrections are based on image unwarping, which is given by the transformation of frequency coordinates into spatial coordinates $\vec{\omega}(\vec{r})$, while intensity corrections are given by the Jacobian determinant $|\partial\vec{\omega}/\partial\vec{r}|$. Commercial use of Jacobian-based approaches to correct distortions due to gradient imperfections works mainly for small deviations of the magnetic field from a constant gradient [10]. The method of imaging with nonlinear encoding coils presented in this study overcomes this limitation and enables the use of all nonlinear magnetic fields that bijectively map spatial coordinates to corresponding frequency coordinates. Furthermore, the corrections are mathematically calculated from analytical expressions for magnetic fields, rather than measured [11,12].

Experimental verification of the reconstruction method for imaging with nonlinear encoding coils was performed only in two dimensions ($D = 2$), while it was also performed in three dimensions ($D = 3$) as a simulation. All three experimental test samples used were also optimized for two-dimensional imaging. They had a thin disk shape, so there was no need to select an imaging slice. This restriction to disk-shaped samples could be overcome by exciting the signal in slices that have the orientation of this disk. This could be done by adding a Maxwell z-gradient coil over the existing nonlinear coils for signal encoding in the xy plane, and in the spin-echo pulse sequence, all hard RF pulses would have to be replaced by shaped soft RF pulses. In general, the use of nonlinear encoding coils for slice selection would result in curved slices of uneven thickness, which is usually undesirable except in special cases. When using nonlinear encoding coils, 3D imaging is more practical than 2D imaging with slice selection.

The simulation of imaging with nonlinear encoding coils in 3D was performed for a very simple set of nonlinear encoding coils. Each of these coils was an infinitely long straight wire, but with a different orientation and position. These wires were arranged in an equilateral triangle, thus forming a logical 3D extension of the experimentally tested 2D nonsymmetric set of encoding coils. For 2D imaging in the

plane of the coils, these coils form an overdetermined system (three frequency components for two spatial coordinates), while in the simulation it was shown that these coils produce magnetic fields that enable relatively efficient imaging in the space above or below this plane. In the simulation, extremely high magnetic field gradients in the imaging region were avoided by choosing an imaging FOV away from the wires, while extremely low magnetic field gradients were avoided by choosing an imaging FOV not too far away from the plane of the wires. In this simulation, the ratio of the FOV to the side of the triangle s was 1:5. This choice also resulted in a Jacobian determinant with the same (negative) sign throughout the FOV, and thus a bijective transformation between the spatial and frequency coordinates. The exception is the plane $z = 0$, where this determinant is zero. For example, if the FOV was shifted along the z axis by $-$FOV/2, the condition of bijectivity of the space-to-frequency transformation would be violated; namely, the spatial coordinates (x,y,z) and $(x,y,-z,)$ would have the same frequency coordinates.

One of our future projects will be an experimental demonstration of the 3D imaging setup in Fig. 4A. This may seem simple and straightforward, but it may not be. The wires (coils) for this experiment should not be infinitely long, but finitely long. This would result in more complex models for the magnetic fields, not to mention the expression for the Jacobian determinant, which is already very complex for infinitely long wires (Eq. (C.4)). Therefore, a completely different approach to modeling will be required. Instead of an analytical approach, numerical modeling will be required. An alternative, perhaps better solution to this problem, would be to map the magnetic fields generated by the encoding coils and use these measurements in image reconstructions.

The Jacobian determinant near zero (the second factor in Eq. (8)) corresponds to regions from where the spatial volume element is transformed into a volume element near zero in the frequency domain. The unwarping procedure for the corresponding regions (the first factor in Eq. (8)) is therefore particularly difficult, since the spatial distribution of the signal has to be reconstructed from a very small spectral element. Unless the spectrum is measured with extremely high resolution, much image resolution is lost, but the SNR is increased. For regions with a high Jacobian determinant, the situation is reversed. The spatial volume element of a such region is transformed into a large volume element in the frequency domain, so that much spatial resolution is gained in the unwarping procedure, but the SNR is decreased. Mathematically, this topic is addressed by the inverse function theorem [31]. Possible ways to overcome the problem of coil non-bijectivity in the space-to-frequency transformation include oversampling by using an additional spatial encoding coil or by using multiple receive coils. An example of the former is the signal acquisition in 4-dimensinal time space, followed by Fourier transformation into a 4-dimensional spectrum and subsequent projection of this along with an unwarping procedure into a 3-dimensional spatial image. Due to the additional dimension, this method can be very time-consuming. From this perspective, a better solution is the second option, i.e., the use of multiple receive coils which is not associated with an increase in scan time.

A problem encountered in the experiments was the vibration of the encoding coils due to a significant torque on them when applying currents. Preliminary measurements of the vibration amplitudes using a projected laser beam reflected from a small mirror attached to the coil showed that the active wire segment displaced by approximately 300 μm at current pulses of 70 A in the case of the nonsymmetric encoding coil [27]. These amplitudes were significantly reduced in further experiments by better fixation of the coil to its holder and also by using a heavier plastic frame in the case of the symmetric coil. The displacements of the encoding coil have the same effect on the image quality as if the coil were stationary and the sample were vibrating with the same amplitude, i.e., motion artifacts are present.

The coil vibration problem could best be solved by designing encoding coils with balanced torque. A simple example of this by modifying existing symmetric encoding coils is shown in Fig. 11A. In the modified design, two additional loops are added to the existing loops at the front. In the added two loops, the direction of the current is the opposite to that the original loops. This has dual effect: first, the desired magnetic field profile $B_z(x,y)$ of the original coil has been extended to a wider area along the z-axis, and second, the torque on the second set of loops is exactly opposite to the torque on the original loops, so that these coils have balanced torque. The coil design in Fig. 11B is an improved version of that in Fig. 11A with three turns of wire, each of slightly larger width. These coils, which resemble the Golay coil in design, have batter uniformity of the magnetic field profile $B_z(x,y)$ along the z-axis than the design in Fig. 11A.

Encoding coils with nonlinear magnetic fields are not yet used in clinical MRI. This could be explained by the underpowered computers in the early days of MRI and much simpler image reconstruction offered by signals encoded with conventional gradient coils than with nonlinear magnetic field coils. Another reason is probably the persistence and convenience of using established technology; in most applications, conventional gradient coils work well and are sufficiently efficient. Conventional gradient coils can be considered a special case of nonlinear gradient coils, so that all the theory presented here also applies to them. Conventional gradient coils are considered the most efficient with respect to the criterion of spatial linearity of the magnetic field (constant gradient).

Integration of the proposed coil design into clinical MRI systems is the ultimate goal, but there are challenges related to B_0 homogeneity, concomitant fields, intravoxel dephasing, local gradients, real-time image reconstruction, and the potential need for new pulse sequences optimized for nonlinear encoding coils. B_0 homogeneity could be affected if the coils are made of magnetic materials or have geometries that locally distort the homogeneity. The other three effects of magnetic field spoiling mentioned above can also degrade the performance of nonlinear encoding coils, especially if these coils are operated with extreme slew rates and gradient amplitudes. Each of these effects requires a more detailed consideration. The image reconstruction burden is expected to be at the level of a typical image reconstruction in parallel imaging. This is because a standard Fourier transform (first step) is followed by image unwarping and intensity corrections (second step). The latter can be performed using a stored space-to-frequency transformation map that is intrinsic to the coil. This map can be measured in

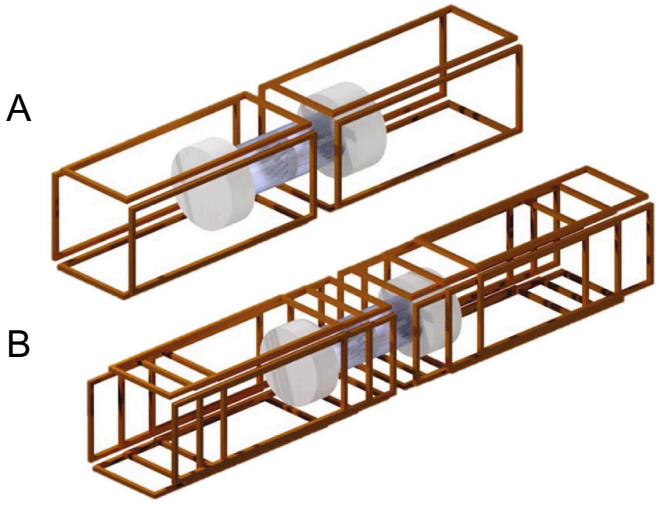

Fig. 11. Improved symmetric nonlinear coil design with square loops with one winding (A) and three windings (B). The coils have better uniformity of magnetic field profile $B_z(x,y)$ along the z-axis and are torque-free during application of current pulses.

some sort of coil calibration process and then used in all subsequent reconstructions in a similar way to how RF coil sensitivity maps are used in parallel imaging. Regarding pulse sequences, practically all existing pulse sequences can be used with nonlinear encoding coils, but their optimization is needed to optimize the operation of the encoding coils, e.g., shorter gradient pulses in longer acquisition loops could be used with encoding coils with low inductance and thus faster gradient switching times.

5. Conclusion

In this study, the performance of different nonlinear coil types for spatial signal encoding was tested experimentally in 2D and by a computer simulation in 3D. All the tested coils share a simple design based on a straight wire as a building block with a highly inhomogeneous magnetic field. The images were reconstructed using our newly presented method for image reconstruction from signals encoded with nonlinear coils. The results of the study confirmed the correctness of the reconstruction method and showed that all tested coil types and their arrangements, despite large differences in the magnetic field of the encoding coils, produce images of similar quality. This has important implications, as it can potentially open up the use of such coils in more advanced MRI systems designed for specific needs, e.g., for faster imaging using nonlinear encoding coils with lower inductance than standard gradient coils, or in new, more patient-friendly MRI systems with less noise or with easier placement or access to the patient.

CRediT authorship contribution statement

Kaja Tušar: Writing – original draft, Software, Methodology, Formal analysis. **Igor Serša:** Writing – original draft, Supervision, Software, Resources, Methodology, Conceptualization.

Declaration of competing interest

The authors declare that they have no known competing financial interests or personal relationships that could have appeared to influence the work reported in this paper.

Acknowledgment

This work was financially supported by the Slovenian Research and Innovation Agency (research core funding No. P1-0060).

Appendix A. Implementation in a spin-echo imaging sequence

The interpretation of Eq. (10) depends on the imaging sequence used. For example, in the case of a standard slice-selective spin-echo imaging sequence, the imaging dimensionality is equal to $D = 2$, where frequency encoding of the signal is used in one dimension and phase encoding of the signal is used in the other dimension. For the frequency-encoding dimension (e.g., the first dimension) the current through the readout coil is constant and equal to the reference current $I_1(t) = I_{ref,1}$ so that the corresponding time component is equal to the actual time

$$t_1 = t \tag{A.1}$$

and $t = 0$ corresponds to the point of the gradient-echo. In the spin-echo imaging sequence, the gradient-echo coincides with the spin-echo of the 90° - 180° RF pulses, so that the signal maximum at the echo time is due to both gradient and spin refocusing. For the phase-encoding dimension (the second dimension), the current I_2 through the coil is applied in a rectangular pulse of duration t_p before the refocusing RF pulse so that the corresponding time component is equal to

$$t_2 = -\frac{I_2 t_p}{I_{ref,2}} \tag{A.2}$$

Note that the negative sign in Eq. (A.2) is due to the application of a current pulse for phase-encoding before the refocusing RF pulse.

Appendix B. Nonlinear spatial encoding coils for 2D MRI based on single (nonsymmetric) or double (symmetric) straight wire segments

The theory of MR imaging with nonlinear magnetic field coils in Eqs. (5)–(8) was verified with two different types of such coils, namely with nonsymmetric and symmetric coils. Both types of coils create magnetic fields B_z by straight wire segments of length $2a$, which are perpendicular to the static magnetic field, have directions along the x or y axis, and are displaced by a distance r from the center of the coordinate system. Nonsymmetric encoding coils have one such segment, while symmetric encoding coils have two such segments placed symmetrically with respect to the center of the coordinate system (Fig. 1). For each type, there are two coils, one with segments along the y axis and the other with the segments along the x axis, which encode signals in the first and second dimension and serve as a replacement for the standard x and y gradient coils, respectively.

The magnetic field per unit current can be calculated using the Biot-Savart law for both types of the encoding nonlinear magnetic field coils and their geometry as given in Fig. 1. For the nonsymmetric encoding coils this is equal to

$$
\begin{aligned}
(B/I)_1\left(x,y\right) &= \frac{\mu_0}{4\pi(x+r)}\left(\frac{y+a}{\sqrt{(y+a)^2+(x+r)^2}}-\frac{y-a}{\sqrt{(y-a)^2+(x+r)^2}}\right)\\
(B/I)_2\left(x,y\right) &= \frac{\mu_0}{4\pi(y+r)}\left(\frac{x+a}{\sqrt{(x+a)^2+(y+r)^2}}-\frac{x-a}{\sqrt{(x-a)^2+(y+r)^2}}\right)
\end{aligned}
\tag{B.1}
$$

and for symmetric encoding coils it is equal to

$$
\begin{aligned}
(B/I)_1\left(x,y\right) &= \frac{\mu_0}{4\pi(x+r)}\left(-\frac{y+a}{\sqrt{(y+a)^2+(x+r)^2}}+\frac{y-a}{\sqrt{(y-a)^2+(x+r)^2}}\right)\\
&\quad+\frac{\mu_0}{4\pi(x-r)}\left(-\frac{y+a}{\sqrt{(y+a)^2+(x-r)^2}}+\frac{y-a}{\sqrt{(y-a)^2+(x-r)^2}}\right)\\
(B/I)_2\left(x,y\right) &= \frac{\mu_0}{4\pi(y+r)}\left(-\frac{x+a}{\sqrt{(x+a)^2+(y+r)^2}}+\frac{x-a}{\sqrt{(x-a)^2+(y+r)^2}}\right)\\
&\quad+\frac{\mu_0}{4\pi(y-r)}\left(-\frac{x+a}{\sqrt{(x+a)^2+(y-r)^2}}+\frac{x-a}{\sqrt{(x-a)^2+(y-r)^2}}\right)
\end{aligned}
\tag{B.2}
$$

To calculate the undistorted reconstructed image using Eq. (8), it is necessary to calculate the corresponding Jacobian determinant

$$
\left|\frac{\partial\vec{\omega}}{\partial\vec{r}}\right| = \begin{vmatrix}\frac{\partial\omega_1}{\partial x} & \frac{\partial\omega_1}{\partial y}\\ \frac{\partial\omega_2}{\partial x} & \frac{\partial\omega_2}{\partial y}\end{vmatrix} = \gamma^2 I_{ref,1} I_{ref,2}\begin{vmatrix}\frac{\partial(B/I)_1}{\partial x} & \frac{\partial(B/I)_1}{\partial y}\\ \frac{\partial(B/I)_2}{\partial x} & \frac{\partial(B/I)_2}{\partial y}\end{vmatrix}
\tag{B.3}
$$

of which elements are partial derivatives of the coil's magnetic field per unit current with respect to x and y coordinates. These are equal to

$$
\begin{aligned}
\frac{\partial(B/I)_1}{\partial x} &= \frac{\mu_0}{4\pi}\left(\frac{1}{(x+r)^2}\left(-\frac{y+a}{\sqrt{(y+a)^2+(x+r)^2}}+\frac{y-a}{\sqrt{(y-a)^2+(x+r)^2}}\right)-\frac{y+a}{\left((y+a)^2+(x+r)^2\right)^{3/2}}+\frac{y-a}{\left((y-a)^2+(x+r)^2\right)^{3/2}}\right)\\
\frac{\partial(B/I)_1}{\partial y} &= \frac{\mu_0}{4\pi(x+r)}\left(\frac{1}{\sqrt{(y+a)^2+(x+r)^2}}-\frac{1}{\sqrt{(y-a)^2+(x+r)^2}}-\frac{(y+a)^2}{\left((y+a)^2+(x+r)^2\right)^{3/2}}+\frac{(y-a)^2}{\left((y-a)^2+(x+r)^2\right)^{3/2}}\right)\\
\frac{\partial(B/I)_2}{\partial x} &= \frac{\mu_0}{4\pi(y+r)}\left(\frac{1}{\sqrt{(x+a)^2+(y+r)^2}}-\frac{1}{\sqrt{(x-a)^2+(y+r)^2}}-\frac{(x+a)^2}{\left((x+a)^2+(y+r)^2\right)^{3/2}}+\frac{(x-a)^2}{\left((x-a)^2+(y+r)^2\right)^{3/2}}\right)\\
\frac{\partial(B/I)_2}{\partial y} &= \frac{\mu_0}{4\pi}\left(\frac{1}{(y+r)^2}\left(-\frac{x+a}{\sqrt{(x+a)^2+(y+r)^2}}+\frac{x-a}{\sqrt{(x-a)^2+(y+r)^2}}\right)-\frac{x+a}{\left((x+a)^2+(y+r)^2\right)^{3/2}}+\frac{x-a}{\left((x-a)^2+(y+r)^2\right)^{3/2}}\right)
\end{aligned}
\tag{B.4}
$$

for nonsymmetric encoding coils and are equal to

$$
\begin{aligned}
\frac{\partial (B/I)_1}{\partial x} &= \frac{\mu_0}{4\pi}\left(\frac{1}{(x+r)^2}\left(\frac{y+a}{\sqrt{(y+a)^2+(x+r)^2}}-\frac{y-a}{\sqrt{(y-a)^2+(x+r)^2}}\right)+\frac{y+a}{\left((y+a)^2+(x+r)^2\right)^{3/2}}-\frac{y-a}{\left((y-a)^2+(x+r)^2\right)^{3/2}}\right)+\\
&\quad\frac{\mu_0}{4\pi}\left(\frac{1}{(x-r)^2}\left(\frac{y+a}{\sqrt{(y+a)^2+(x-r)^2}}-\frac{y-a}{\sqrt{(y-a)^2+(x-r)^2}}\right)+\frac{y+a}{\left((y+a)^2+(x-r)^2\right)^{3/2}}-\frac{y-a}{\left((y-a)^2+(x-r)^2\right)^{3/2}}\right)\\
\frac{\partial (B/I)_1}{\partial y} &= \frac{\mu_0}{4\pi(x+r)}\left(-\frac{1}{\sqrt{(y+a)^2+(x+r)^2}}+\frac{1}{\sqrt{(y-a)^2+(x+r)^2}}+\frac{(y+a)^2}{\left((y+a)^2+(x+r)^2\right)^{3/2}}-\frac{(y-a)^2}{\left((y-a)^2+(x+r)^2\right)^{3/2}}\right)+\\
&\quad\frac{\mu_0}{4\pi(x-r)}\left(-\frac{1}{\sqrt{(y+a)^2+(x-r)^2}}+\frac{1}{\sqrt{(y-a)^2+(x-r)^2}}+\frac{(y+a)^2}{\left((y+a)^2+(x-r)^2\right)^{3/2}}-\frac{(y-a)^2}{\left((y-a)^2+(x-r)^2\right)^{3/2}}\right)\\
\frac{\partial (B/I)_2}{\partial x} &= \frac{\mu_0}{4\pi(y+r)}\left(-\frac{1}{\sqrt{(x+a)^2+(y+r)^2}}+\frac{1}{\sqrt{(x-a)^2+(y+r)^2}}+\frac{(x+a)^2}{\left((x+a)^2+(y+r)^2\right)^{3/2}}-\frac{(x-a)^2}{\left((x-a)^2+(y+r)^2\right)^{3/2}}\right)+\\
&\quad\frac{\mu_0}{4\pi(y-r)}\left(-\frac{1}{\sqrt{(x+a)^2+(y-r)^2}}+\frac{1}{\sqrt{(x-a)^2+(y-r)^2}}+\frac{(x+a)^2}{\left((x+a)^2+(y-r)^2\right)^{3/2}}-\frac{(x-a)^2}{\left((x-a)^2+(y-r)^2\right)^{3/2}}\right)\\
\frac{\partial (B/I)_2}{\partial y} &= \frac{\mu_0}{4\pi}\left(\frac{1}{(y+r)^2}\left(\frac{x+a}{\sqrt{(x+a)^2+(y+r)^2}}-\frac{x-a}{\sqrt{(x-a)^2+(y+r)^2}}\right)+\frac{x+a}{\left((x+a)^2+(y+r)^2\right)^{3/2}}-\frac{x-a}{\left((x-a)^2+(y+r)^2\right)^{3/2}}\right)+\\
&\quad\frac{\mu_0}{4\pi}\left(\frac{1}{(y-r)^2}\left(\frac{x+a}{\sqrt{(x+a)^2+(y-r)^2}}-\frac{x-a}{\sqrt{(x-a)^2+(y-r)^2}}\right)+\frac{x+a}{\left((x+a)^2+(y-r)^2\right)^{3/2}}-\frac{x-a}{\left((x-a)^2+(y-r)^2\right)^{3/2}}\right)
\end{aligned}
\tag{B.5}
$$

for symmetric encoding coils.

Appendix C. Nonlinear spatial encoding coils for 3D MRI based on three infinitely long straight wires

According to the presented theory in subsection 2.1, MR imaging with nonlinear spatial encoding coils is possible by using three different such coils, when a non-zero Jacobian determinant belongs to the conversion of these coils from spatial coordinate to frequency in the imaging region. A direct consequence of this is that this determinant has the same sign in this region. For an example of such imaging, let us take three infinitely long straight wires as sources of nonlinear encoding fields. The z-component of the magnetic field per unit current of an infinitely long straight wire at a spatial point $\vec{r}$ is given by

$$
(B/I)_i = \frac{\mu_0\left(\vec{e}_i\times\vec{r}_{\perp i}\right)\cdot\vec{e}_z}{2\pi\left|\vec{r}_{\perp i}\right|^2}\quad,\quad \vec{r}_{\perp i}=\vec{r}-\vec{a}_i-\left(\left(\vec{r}-\vec{a}_i\right)\cdot\vec{e}_i\right)\vec{e}_i \tag{C.1}
$$

Here $\vec{r}_{\perp i}$ is the perpendicular vector to the wire to the point $\vec{r}$, $\vec{a}_i$ is the vector from the origin of the coordinate system to the i-th wire and $\vec{e}_i$ is the unit vector with the direction of the wire and the current through it. An illustration of these vectors relative to a straight wire is shown in Fig. 4B.

In this study, a simple case is considered where the wires are all in the same plane, namely the xy plane at $z=0$. The wires form an equilateral triangle with side s, centered at the origin of the coordinate system, and the currents through the wires flow in a counterclockwise direction (Fig. 4A). The corresponding parameters of the model in Eq. (C.1) for these wires are $\vec{e}_1=(1,0,0)$, $\vec{e}_2=\left(-\frac{1}{2},\frac{\sqrt{3}}{2},0\right)$, $\vec{e}_3=\left(-\frac{1}{2},-\frac{\sqrt{3}}{2},0\right)$, and $\vec{a}_1=\left(0,-\frac{1}{2\sqrt{3}}s,0\right)$, $\vec{a}_2=\left(\frac{1}{4}s,\frac{1}{4\sqrt{3}}s,0\right)$, $\vec{a}_3=\left(-\frac{1}{4}s,\frac{1}{4\sqrt{3}}s,0\right)$, which yield

$$
\begin{aligned}
(B/I)_1 &= \frac{\mu_0\left(y+\frac{1}{2\sqrt{3}}s\right)}{2\pi\left(\left(y+\frac{1}{2\sqrt{3}}s\right)^2+z^2\right)}\\
(B/I)_2 &= \frac{\mu_0\left(-\frac{1}{2}y-\frac{\sqrt{3}}{2}x+\frac{1}{2\sqrt{3}}s\right)}{2\pi\left(\left(\frac{3}{4}x+\frac{\sqrt{3}}{4}y-\frac{1}{4}s\right)^2+\left(\frac{1}{4}y+\frac{\sqrt{3}}{4}x-\frac{1}{4\sqrt{3}}s\right)^2+z^2\right)}\\
(B/I)_3 &= \frac{\mu_0\left(-\frac{1}{2}y+\frac{\sqrt{3}}{2}x+\frac{1}{2\sqrt{3}}s\right)}{2\pi\left(\left(\frac{3}{4}x-\frac{\sqrt{3}}{4}y+\frac{1}{4}s\right)^2+\left(\frac{1}{4}y-\frac{\sqrt{3}}{4}x-\frac{1}{4\sqrt{3}}s\right)^2+z^2\right)}
\end{aligned}
\tag{C.2}
$$

For the encoding magnetic fields in Eq. (C.2) for three-dimensional imaging, the corresponding Jacobian determinant can also be calculated

$$
\left|\frac{\partial\vec{\omega}}{\partial\vec{r}}\right| = \begin{vmatrix} \frac{\partial\omega_1}{\partial x} & \frac{\partial\omega_1}{\partial y} & \frac{\partial\omega_1}{\partial z} \\ \frac{\partial\omega_2}{\partial x} & \frac{\partial\omega_2}{\partial y} & \frac{\partial\omega_2}{\partial z} \\ \frac{\partial\omega_3}{\partial x} & \frac{\partial\omega_3}{\partial y} & \frac{\partial\omega_3}{\partial z} \end{vmatrix} = \gamma^3 I_{ref,1}I_{ref,2}I_{ref,3} \begin{vmatrix} \frac{\partial(B/I)_1}{\partial x} & \frac{\partial(B/I)_1}{\partial y} & \frac{\partial(B/I)_1}{\partial z} \\ \frac{\partial(B/I)_2}{\partial x} & \frac{\partial(B/I)_2}{\partial y} & \frac{\partial(B/I)_2}{\partial z} \\ \frac{\partial(B/I)_3}{\partial x} & \frac{\partial(B/I)_3}{\partial y} & \frac{\partial(B/I)_3}{\partial z} \end{vmatrix}
\tag{C.3}
$$

which, according to Eq. (C.3), is equal to

$$
\left|\frac{\partial\vec{\omega}}{\partial\vec{r}}\right| = -\left(\frac{\gamma\mu_0}{2\pi}\right)^3 I_{ref,1}I_{ref,2}I_{ref,3}\cdot
\frac{31104z\left(s^5+6\sqrt{3}s^2y(-3x^2+y^2)-18\sqrt{3}y(-3x^2+y^2)(x^2+y^2-4z^2)-12s^3(x^2+y^2+2z^2)+9s(3x^4+6x^2y^2+3y^4+16z^4)\right)}{\left(s^2+6sx+9x^2-2\sqrt{3}sy-6\sqrt{3}xy+3y^2+12z^2\right)^2\left(s^2+4\sqrt{3}sy+12(y^2+z^2)\right)^2\left(s^2-2s(3x+\sqrt{3}y)+3(3x^2+2\sqrt{3}xy+y^2+4z^2)\right)^2}
\tag{C.4}
$$

The Jacobian determinant in Eq. (C.4) was calculated using Wolfram Mathematica analytical solver (Wolfram Research, Champaign, IL, USA).

Data availability

Data will be made available on request.

References

[1] P.C. Lauterbur, Image formation by induced local interactions: examples of employing nuclear magnetic resonance, Nature 242 (1973) 190–191.
[2] A. Kumar, D. Welti, R.R. Ernst, Nmr Fourier Zeugmatography, J. Magn. Reson. 18 (1975) 69–83.
[3] D.K. Sodickson, W.J. Manning, Simultaneous acquisition of spatial harmonics (SMASH): fast imaging with radiofrequency coil arrays, Magn. Reson. Med. 38 (1997) 591–603.
[4] K.P. Pruessmann, M. Weiger, M.B. Scheidegger, P. Boesiger, SENSE: sensitivity encoding for fast MRI, Magn. Reson. Med. 42 (1999) 952–962.
[5] M.A. Griswold, P.M. Jakob, R.M. Heidemann, M. Nittka, V. Jellus, J. Wang, B. Kiefer, A. Haase, Generalized autocalibrating partially parallel acquisitions (GRAPPA), Magn. Reson. Med. 47 (2002) 1202–1210.
[6] J. Hennig, A.M. Welz, G. Schultz, J. Korvink, Z. Liu, O. Speck, M. Zaitsev, Parallel imaging in non-bijective, curvilinear magnetic field gradients: a concept study, MAGMA 21 (2008) 5–14.
[7] G. Schultz, P. Ullmann, H. Lehr, A.M. Welz, J. Hennig, M. Zaitsev, Reconstruction of MRI data encoded with arbitrarily shaped, curvilinear, nonbijective magnetic fields, Magn. Reson. Med. 64 (2010) 1390–1403.
[8] J.P. Stockmann, P.A. Ciris, G. Galiana, L. Tam, R.T. Constable, O-space imaging: highly efficient parallel imaging using second-order nonlinear fields as encoding gradients with no phase encoding, Magn. Reson. Med. 64 (2010) 447–456.
[9] H. Wang, L.K. Tam, R.T. Constable, G. Galiana, Fast rotary nonlinear spatial acquisition (FRONSAC) imaging, Magn. Reson. Med. 75 (2016) 1154–1165.
[10] G.H. Glover, N.J. Pelc, Method for correcting image distortion due to gradient nonuniformity, in: U.S. Patent (Ed.), General Electric Company, Milwaukee, Wis, USA, 1986, p. 6.
[11] S.J. Doran, L. Charles-Edwards, S.A. Reinsberg, M.O. Leach, A complete distortion correction for MR images: I. Gradient warp correction, Phys. Med. Biol. 50 (2005) 1343–1361.
[12] B.M. Whelan, P.Z.Y. Liu, S. Shan, D.E.J. Waddington, B. Dong, M.G. Jameson, P. J. Keall, Open-source hardware and software for the measurement, characterization, reporting, and correction of geometric distortion in MRI, Med. Phys. 51 (2024) 8399–8410.
[13] K. Selvaganesan, Y. Ha, H. Sun, Z. Zhang, C. Sun, A. Samardzija, G. Galiana, R. T. Constable, Encoding scheme design for gradient-free, nonlinear projection imaging using Bloch-Siegert RF spatial encoding in a low-field, open MRI system, Sci. Rep. 14 (2024) 3307.
[14] K. Selvaganesan, Y. Wan, Y. Ha, B. Wu, K. Hancock, G. Galiana, R.T. Constable, Magnetic resonance imaging using a nonuniform Bo (NuBo) field-cycling magnet, PLoS One 18 (2023) e0287344.
[15] S.Y. Lee, Z.H. Cho, Localized volume selection technique using an additional radial gradient coil, Magn. Reson. Med. 12 (1989) 56–63.
[16] E. Hoque Bhuiyan, A. Dewdney, J. Weinreb, G. Galiana, Feasibility of diffusion weighting with a local inside-out nonlinear gradient coil for prostate MRI, Med. Phys. 48 (2021) 5804–5818.
[17] H. Weber, D. Gallichan, G. Schultz, C.A. Cocosco, S. Littin, W. Reichardt, A. Welz, W. Witschey, J. Hennig, M. Zaitsev, Excitation and geometrically matched local encoding of curved slices, Magn. Reson. Med. 69 (2013) 1317–1325.
[18] H. Weber, M. Haas, D. Kokorin, D. Gallichan, J. Hennig, M. Zaitsev, Local shape adaptation for curved slice selection, Magn. Reson. Med. 72 (2014) 112–123.
[19] F.J. Rybicki, S. Patz, M.I. Hrovat, Y.M. Pulyer, Reconstruction algorithm for novel ultrafast magnetic resonance imaging, Int. J. Imaging Syst. Technol. 10 (1999) 209–215.
[20] S. Patz, M.I. Hrovat, Y.M. Pulyer, F.J. Rybicki, Novel encoding technology for ultrafast MRI in a limited spatial region, Int. J. Imaging Syst. Technol. 10 (1999) 216–224.
[21] S. Littin, D. Gallichan, A.M. Welz, F. Jia, A. Dewdney, H. Weber, G. Schultz, J. Hennig, M. Zaitsev, Monoplanar gradient system for imaging with nonlinear gradients, MAGMA 28 (2015) 447–457.
[22] M. Zaitsev, G. Schultz, J. Hennig, R. Gruetter, D. Gallichan, Parallel imaging with phase scrambling, Magn. Reson. Med. 73 (2015) 1407–1419.
[23] L.K. Tam, J.P. Stockmann, G. Galiana, R.T. Constable, Null space imaging: nonlinear magnetic encoding fields designed complementary to receiver coil sensitivities for improved acceleration in parallel imaging, Magn. Reson. Med. 68 (2012) 1166–1175.
[24] D. Gallichan, C.A. Cocosco, A. Dewdney, G. Schultz, A. Welz, J. Hennig, M. Zaitsev, Simultaneously driven linear and nonlinear spatial encoding fields in MRI, Magn. Reson. Med. 65 (2011) 702–714.
[25] N.L. Dispenza, S. Littin, M. Zaitsev, R.T. Constable, G. Galiana, Clinical potential of a new approach to MRI acceleration, Sci. Rep. 9 (2019).

[26] Y. Rodriguez, N.M.H. Elsaid, B. Keil, G. Galiana, 3D FRONSAC with PSF reconstruction, J. Magn. Reson. 355 (2023) 107544.
[27] K. Tusar, I. Sersa, Use of nonlinear pulsed magnetic fields for spatial encoding in magnetic resonance imaging, Sci. Rep. 14 (2024) 7521.
[28] P.T. Callaghan, J. Stepisnik, Spatially-distributed pulsed gradient spin-Echo Nmr using single-wire proximity, Phys. Rev. Lett. 75 (1995) 4532–4535.
[29] Z. Wang, A.C. Bovik, H.R. Sheikh, E.P. Simoncelli, Image quality assessment: from error visibility to structural similarity, IEEE Trans. Image Process. 13 (2004) 600–612.
[30] R.C. Gonzalez, R.E. Woods, Digital image processing, Prentice Hall, Upper Saddle River, N.J, 2002.
[31] L. Hörmander, The Analysis of Linear Partial Differential Operators, Springer, Berlin ; New York, 2003.